Urban Climate 68 (2026) 103050

Contents lists available at ScienceDirect

Urban Climate

journal homepage: www.elsevier.com/locate/uclim

Impact of Kuala Lumpur as a tropical city on cloud formation: Numerical experiments using the WRF-UCM model

Sharifah Faridah Syed Mahbar [a,b], Nobuyasu Suzuki [c], Hiroyuki Kusaka [c,*]

[a] Graduate School of Life and Environmental Sciences, University of Tsukuba, Japan
[b] Malaysian Meteorological Department, Petaling Jaya, Selangor, Malaysia
[c] Center for Computational Sciences, University of Tsukuba, Japan

A R T I C L E I N F O

Keywords:
Urban cloud
Urban heat island
Atmospheric boundary layer
Tropical city
Kuala Lumpur

A B S T R A C T

Previous satellite-based studies have shown that Greater Kuala Lumpur (GKL) consistently exhibits a higher cloud frequency than surrounding rural areas. To investigate the underlying mechanisms, numerical experiments were conducted using the Weather Research and Forecasting (WRF) model for 227 hot days without daytime precipitation during the wet season (DJF) and 141 hot days without daytime precipitation during the dry season (JJA). The results show that urbanised areas within GKL exhibit higher sensible heat fluxes and deeper boundary layers than surrounding rural regions. Despite lower latent heat fluxes and reduced near-surface relative humidity, which would normally suppress cloud formation by raising the lifting condensation level (LCL), cloud frequency is enhanced over GKL. This enhancement can be explained by two mechanisms. First, the deeper urban boundary layer largely offsets the negative effect of an elevated LCL. Second, urban heat island and modified sea-breeze circulations enhance moisture advection from surrounding rural areas and adjacent oceans, increasing moisture within the urban boundary layer. The spatial distribution of urban-induced cloud frequency exhibits a clear seasonal dependence. During DJF, the enhancement extends across the GKL region, whereas during JJA it is mainly confined to inland urban areas. Areas of enhanced horizontal moisture flux convergence closely correspond to increased cloud frequency. These seasonal differences suggest that urbanisation modifies interactions among the background monsoonal flow, sea-breeze circulation, and urban heat island circulation, thereby altering the location and intensity of moisture convergence and the associated cloud response. These findings provide new insights into urban-induced cloud formation in tropical cities.

1. Introduction

Land-use and land-cover modifications associated with urbanisation represent a significant anthropogenic forcing that alters regional atmospheric processes, with important implications for cloud formation and precipitation patterns (IPCC, 2021; Pielke Sr et al., 2011). By modifying surface energy balance, moisture availability, and aerodynamic roughness, urban environments influence boundary-layer development, mesoscale circulations, and convective processes that govern cloud evolution (Oke, 1982; Shepherd, 2005). These changes can lead to measurable anomalies in precipitation characteristics, including variations in rainfall

* Corresponding author at: Center for Computational Sciences, University of Tsukuba, 1-1-1 Tennodai, Tsukuba, Ibaraki 305-8577, Japan.
E-mail addresses: faridah_mahbar@met.gov.my (S.F. Syed Mahbar), kusaka@ccs.tsukuba.ac.jp (H. Kusaka).

https://doi.org/10.1016/j.uclim.2026.103050
Received 1 August 2025; Received in revised form 16 June 2026; Accepted 9 July 2026

intensity, spatial distribution, and timing, both within and downwind of urban areas across a wide range of climatic regimes, including temperate (e.g., Fujibe et al., 2009; Shepherd et al., 2010; Miao et al., 2011; Kusaka et al., 2014, 2019; Niyogi et al., 2017; Aota and Kusaka, 2026) and tropical climates (e.g., Lin et al., 2008, 2011; Doan et al., 2021; Li et al., 2022; Hasebe et al., 2026). Recent regional studies have demonstrated that urban-induced precipitation responses are not uniform but depend on background climate and meteorological conditions and urban morphology (Sui et al., 2024; Pryor et al., 2025). Such findings highlight the need to better understand the physical linkages between urban land-cover modification, cloud development, and precipitation processes, particularly in rapidly urbanising regions where these interactions remain insufficiently explored. Recent studies suggest that urban environments enhance precipitation through both land-surface processes and aerosol–cloud interactions, with the latter playing an important role in urban precipitation variability (Moraglia et al., 2024; Moraglia and Crippa, 2026).

Given the fundamental role of cloud cover and frequency in regulating climate variability and precipitation processes, investigating urban influences on cloud formation provides a key pathway for understanding these interactions (Stephens, 2005; Rosenfeld et al., 2014; Gettelman and Sherwood, 2016). This can be achieved through various approaches, including observational tools, statistical analyses, and advanced numerical experiments, all of which are crucial for understanding the processes governing cloud formation, particularly in urbanised areas. Nevertheless, studies specifically focusing on urban cloud formation remain limited compared with the extensive literature on urban influences on precipitation (Theeuwes et al., 2019, 2022).

One of the earliest observational studies on urban cloud formation, conducted by Landsberg (1981), examined the effects of urbanisation on cloud development. His analysis of cloud frequency over New York City demonstrated that midday cloud cover during summer was consistently higher over an urban airfield than over a nearby rural site. The study also highlighted the combined effects of the heat island phenomenon, surface roughness, and the presence of hygroscopic condensation nuclei in shaping urban cloud microphysics, dynamics, and precipitation patterns.

Subsequent research has built upon Landsberg's findings using a range of observational approaches. Ground-based remote sensing techniques, such as wind profilers, ceilometers, and airborne lidar, have been employed to investigate cloud properties and boundary-layer dynamics. For instance, Angevine et al. (2003) utilized these tools over Nashville to assess urban influences on mixing height and cloud fraction, reinforcing the notion that urban areas experience enhanced cloud formation compared with their rural surroundings. Danchovski (2024) Employed ceilometer observations in Sofia, demonstrating that during the warm season, cloud-base heights over the city Centre exceeded those over the periphery by approximately 200 m in the afternoon, reflecting the impact of urban heating and local convection. Moriwaki et al. (2013) Also used ceilometer observations to demonstrate that cloud-base heights over a medium-sized Japanese city were higher than those over the surrounding suburban areas. Satellite-based remote sensing has further substantiated these urban cloud effects on a broader scale. Romanov (1999) Observed increased cloud development over Moscow, while Theeuwes et al. (2019) documented similar trends over Paris and London. Vo et al. (2023) Reported enhanced daytime cloud cover in both summer and winter over most U.S. cities. During nighttime, cloud cover increased by up to 5.8% in summer but showed slight suppression in winter.

Numerical experiments provide a robust means of uncovering the mechanisms driving these contrasts in cloud formation. For example, Kanda et al. (2001) and Inoue and Kimura (2007) demonstrated that urban areas exhibit higher cloud fractions and sensible heat fluxes than rural regions. In particular, Inoue and Kimura (2007) found that small cumulus clouds were more frequent over urban areas but less common over suburban and rural settings. Further studies by Kang and Bryan (2011) revealed that cloud-base height over warmer surfaces increases with surface heterogeneity. Based on the findings of cloud presence over London (Theeuwes et al., 2019), Theeuwes et al. (2022) demonstrated that urban heat circulations promote moisture convergence and upward air motion over London under low-wind-speed conditions. Such land-use perturbation approaches, in which urban grids are replaced by surrounding rural land-cover types, have been widely used to isolate urban effects on clouds and precipitation across a variety of climatic regions worldwide.

Syed Mahbar and Kusaka (2024a) conducted a statistical study of urban cloud enhancement in the greater Kuala Lumpur (GKL) region using Himawari-8 satellite observations, which revealed that urban areas consistently exhibit greater cloud cover than rural areas. This distinct urban–rural contrast is particularly evident at 15:00 local time (LT), with cloud-cover ratios of 1.22 during the southwest monsoon and 1.24 during the northeast monsoon. Building on this research, we conducted numerical experiments to investigate the impact of urban areas on cloud formation, with the aim of identifying differences in cloud presence and examining how variations in the surface heat budget contribute to the increased cloud cover observed over GKL.

The mechanisms driving urban cloud enhancement in tropical cities such as GKL, which experience distinct meteorological conditions, including high solar radiation and abundant moisture, have not been explored in depth through numerical simulations. Furthermore, how these urban cloud enhancement processes and their spatial distribution vary under changing monsoonal seasons remains a critical gap. This study aims to fill this gap by providing new insights into the mechanisms of urban cloud formation and their implications for urban weather and climate. To the best of our knowledge, this study is the first numerical investigation of urban cloud enhancement in a southeast Asian city.

2. Methods and data

2.1. Study area – GKL

As of 2023, Greater Kuala Lumpur (GKL), Malaysia's primary rapidly expanding urban agglomeration, is home to 22% of the nation's population (Public Sector Open Data, 2024), making it a densely populated region vulnerable to various urban hazards, including extreme heat, severe thunderstorms, and flash flooding. The region's climate is influenced by the Asian-Australian monsoon system and prevailing wind patterns (Jamaluddin et al., 2018; Morris et al., 2017; Tangang et al., 2017; Ramakreshnan et al., 2019; Mohammad Hamray and Choi, 2022). The southwest monsoon, characterised by south-westerly winds, occurs from June to August (JJA), while the northeast monsoon, dominated by north-easterly winds, spans from December to February (DJF). The inter-monsoon period bridges these two seasons.

Situated on the west coast of Peninsular Malaysia, GKL is bordered by the Strait of Malacca to the west and the Titiwangsa Mountain Range to the east, as illustrated in Fig. 1. It comprises ten local government areas, including the Kuala Lumpur metropolitan city, the Putrajaya administrative capital, and the local authority regions of Petaling Jaya, Subang Jaya, Shah Alam, Ampang Jaya, Selayang, Kajang, Klang, and Sepang (Syed Mahbar and Kusaka, 2024b). Rapid urbanisation in Kuala Lumpur has driven development beyond the city's core, forming a sprawling urban agglomeration covering 2793 km^2 (Yasin et al., 2022), encompassing the Kuala Lumpur Federal Territory and parts of Selangor. A distinctive feature of GKL is the presence of two major rivers, the Klang and Gombak Rivers, which flow through the city and shape its geographical identity (Bhuiyan et al., 2018).

2.2. Selection of simulation cases

To investigate the influence of urbanisation on cloud formation, WRF simulations were conducted for the cases identified by Syed Mahbar and Kusaka (2024a). The selected cases correspond to high-temperature days without daytime precipitation over Greater Kuala Lumpur (GKL) and its surrounding areas, thereby excluding precipitation events primarily associated with large-scale convective disturbances. Following Syed Mahbar and Kusaka (2024a), high-temperature days were defined using the 80th-percentile temperature threshold calculated separately for DJF and JJA. The resulting dataset consists of 227 cases during DJF and 141 cases during JJA. The surface air temperature and precipitation data used for event selection were obtained from observations conducted by the Malaysian Meteorological Department. Fig. 2 shows the spatial distribution of cloud occurrence frequency for the selected cases analysed in this study.

This study continues to define DJF as the wet season, rather than the November–March period designated by the Malaysian Meteorological Department (MET Malaysia). DJF was widely recognised in the research community as a representative period for Malaysia's wet season (e.g., Shariff et al., 2015; Tangang et al., 2017; Jamaluddin et al., 2018; Tangang et al., 2020; Jamaluddin et al., 2022; An et al., 2023; Syed Mahbar and Kusaka, 2024a).

2.3. Model configuration and experimental design

The Weather Research and Forecasting (WRF) model (version 4.3.3) (Skamarock et al., 2019), coupled with a single-layer Urban

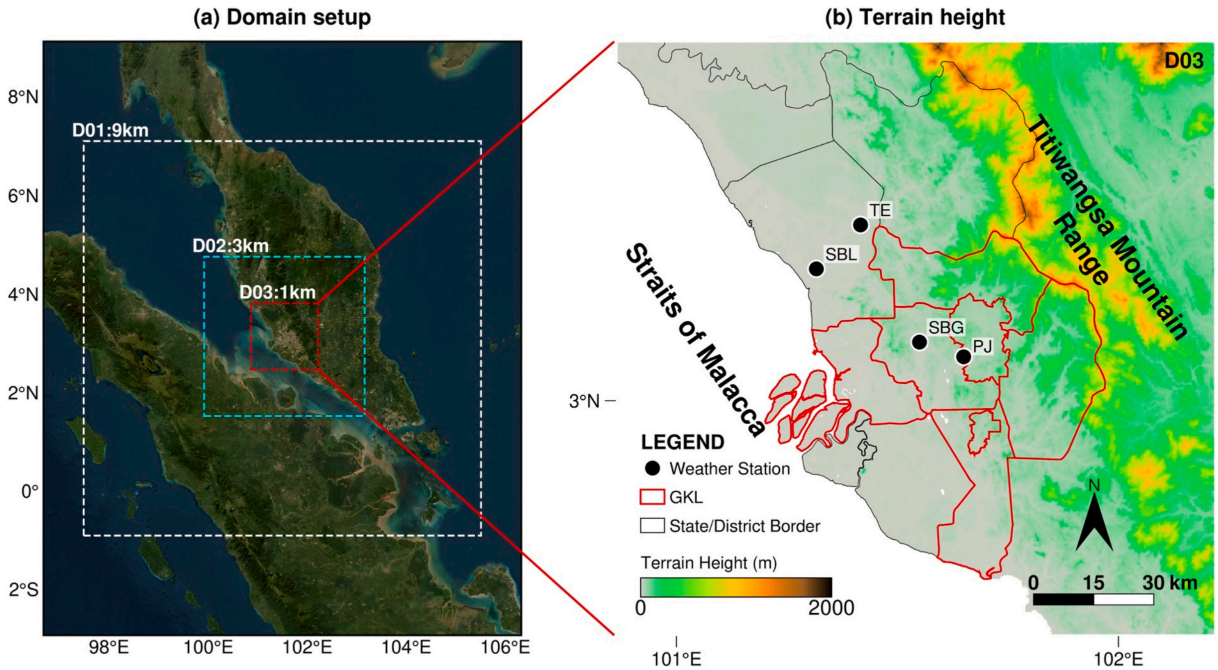

Fig. 1. Study area. (a) Nested domains used in the WRF model for the GKL region, showing three domain setups with resolutions of 9 km (D01), 3 km (D02), and 1 km (D03). (b) Zoomed-in view of the innermost domain (D03), highlighting terrain height, shaded from green to brown, represent low to high elevation. The locations of weather stations used for verification and analysis are shown: Petaling Jaya (PJ), Subang (SBG), Sg. Buloh (SBL), and Tennamaran Estate (TE). The fuzzy red lines indicate the GKL boundary, while black lines mark state/district. (For interpretation of the references to colour in this figure legend, the reader is referred to the web version of this article.)

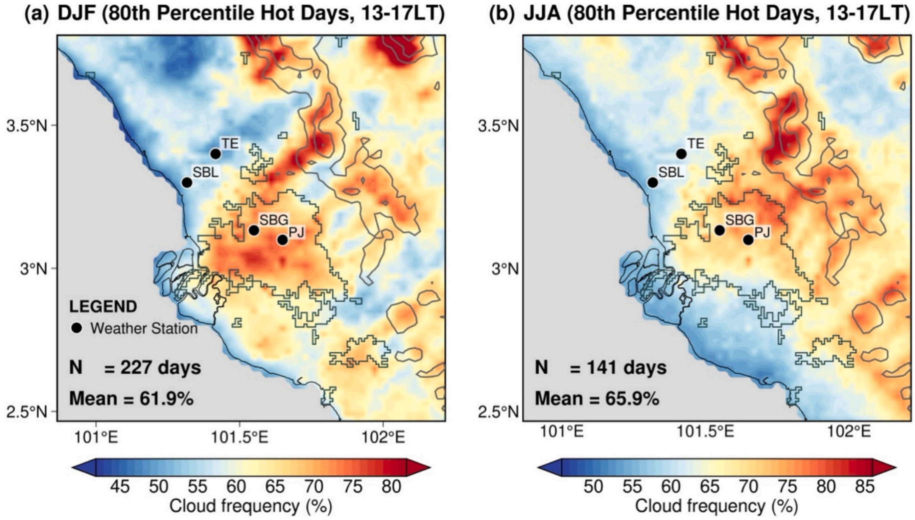

Fig. 2. Spatial distribution of cloud frequency (%) at 13:00–17:00 LT based on Himawari-8 satellite data for the period 2016–2021. Panels (a) and (b) show the results for 80th percentile hot days during DJF and JJA, respectively. Meteorological stations are indicated by circles, including Petaling Jaya (PJ), Subang (SBG), Sg. Buloh (SBL), and Tennamaran Estate (TE). Grey contours indicate terrain elevation at 500 m intervals, while the dashed black line outlines the urban area. The lower-right corner of each panel shows the number of analysed days and the domain-mean cloud frequency (%).

Canopy Model (WRF-UCM) (Kusaka et al., 2001; Kusaka and Kimura, 2004; Chen et al., 2011), was used in this study. The single-layer UCM represents urban street-canyon geometry and urban material properties, and calculates roof, wall, and road surface temperatures, as well as surface heat and momentum fluxes.

In the standard WRF-UCM officially released by NCAR, urban areas are classified into three or ten urban categories, and urban parameters such as urban fraction and anthropogenic heat flux are prescribed for each category. In contrast, the WRF-UCM used in this study was modified to directly ingest grid-by-grid two-dimensional (2D) distributions of urban area fraction and anthropogenic heat flux. Similar 2D extensions of the WRF-UCM framework have been successfully implemented in previous studies (e.g., Lin et al., 2016; Doan and Kusaka, 2018; Doan et al., 2019; Aota and Kusaka, 2026; Hasebe et al., 2026).

The physical parameterisation schemes used in the numerical simulations are listed in Table 1 and follow the operational validation guidelines and baseline configurations documented in the Technical Note published by the Malaysian Meteorological Department (MET Malaysia) (Yusof, 2022). Among these schemes, cloud microphysics plays a key role in representing cloud formation and precipitation processes and is known to strongly influence simulated precipitation, particularly in convection-permitting simulations (Jankov et al., 2005; Morrison et al., 2009). In this study, the Thompson microphysics scheme was adopted as the baseline configuration because it provides a balanced representation of mixed-phase cloud processes while maintaining computational efficiency for regional-scale applications (Thompson et al., 2008). This configuration is also consistent with that used by Syed Mahbar and Kusaka (2024b), who demonstrated satisfactory performance in reproducing urban thermal environments and boundary-layer processes. To assess the robustness of the simulated urban cloud response to the choice of microphysics parameterisation, additional simulations were conducted using the Milbrandt–Yau double-moment microphysics scheme (Milbrandt and Yau, 2005a, 2005b).

Table 1
Model configuration.

Model version: WRF4.3.3-ARW			
Parent Data	NCEP GDAS/FNL (6-hourly data; 0.25° spatial resolution)		
SST Data	OISST ver. 2.1 (daily; 0.25° horizontal resolution)		
Domain	D01	DO2	DO3
Grid spacing (km)	9	3	1
Grid cell numbers	100 × 100	121 × 121	151 × 151
No. of vertical layers	34		
Land Surface Model	Noah-MP Land Surface Model (Niu et al., 2011; Yang et al., 2011)		
Urban Canopy Model	Single-layer UCM (Chen et al., 2011; Kusaka et al., 2001; Kusaka and Kimura, 2004)		
Microphysics	Thompson Scheme (Thompson et al., 2008)		
Planetary Boundary Layer	Mellor-Yamada Nakanishi Niino Level 2.5 (Nakanishi and Niino, 2006, 2009)		
Shortwave Radiation	Dudhia Shortwave Scheme (Dudhia, 1989)		
Longwave Radiation	RRTM Longwave Scheme (Mlawer et al., 1997)		
Cumulus	New Tiedtke Scheme (Zhang and Wang, 2017)	–	–

Three nested model domains centred on Kuala Lumpur were configured with horizontal grid resolutions of 9 km, 3 km, and 1 km (Fig. 1). The outermost domain, consisting of 100 × 100 grid cells, was designed to adequately capture synoptic-scale conditions provided by the NCEP Global Data Assimilation System Final (GDAS/FNL) analysis while maintaining computational efficiency. Although the model domain is relatively limited in spatial extent, the three-level nesting configuration ensures that the innermost analysis domain remains sufficiently distant from the lateral boundaries, thereby minimising boundary effects on simulated urban-scale processes (Skamarock et al., 2019). This configuration is suitable for investigating urban-scale processes rather than large-scale circulation features. Lateral boundary conditions were provided by the FNL dataset at 0.25° spatial resolution and 6-h temporal intervals. Sea surface temperature (SST) fields were obtained from the NOAA Daily Optimum Interpolation Sea Surface Temperature (OISST) version 2.1 dataset (Huang et al., 2021) and updated daily throughout the simulations. Each simulation included a 16-h spin-up period.

Urban representation followed the baseline methodology of Syed Mahbar and Kusaka (2024b), whose configuration has been demonstrated to perform reliably in simulating extreme high-temperature conditions. The urban surface parameters used in this study are summarised in Table 2 and were established based on Morris et al. (2016).

This study used the "High Resolution Land-Use and Land Cover Map of Southeast Asia in 2023" (HRLULC-SEA) dataset developed by the JAXA Earth Observation Research Center (EORC). This advanced dataset characterises forest canopies with superior precision, distinguishing evergreen and deciduous forests from agricultural plantation croplands. To incorporate HRLULC-SEA into WRF, the original land-use classes were reclassified according to the conversion rules summarised in Table 3.

Fig. 3 presents the land-use data used in WRF (HRLULC-SEA), including the modifications applied to the urban (URB) and no urban (noURB) scenarios, together with the horizontally distributed two-dimensional (2D) urban fraction and anthropogenic heat emission (AHE) datasets used in the URB scenario. For the noURB scenario, urban grid cells were replaced with the dominant surrounding rural land-use type, namely the Cropland/Woodland Mosaic category, and no anthropogenic heat emissions (AHE) were prescribed. All other land-use classifications were kept identical to those in the URB scenario to isolate the effects of urban land use on local cloud-forming processes. This approach, in which urban grid cells are replaced by neighbouring rural vegetation types, has been widely used to quantify the impacts of urbanisation and urban heat island intensity while minimising changes in large-scale meteorological conditions (e.g., Miao et al., 2011; Han et al., 2014; Kusaka et al., 2014; Chew et al., 2020; Ghielmini et al., 2024; Moraglia et al., 2024; Syed Mahbar and Kusaka, 2024b; Aota and Kusaka, 2026; Hasebe et al., 2026). The main differences between the URB and noURB scenarios are summarised in Table 4.

Anthropogenic heat emissions (AHE) is defined as the sum of building heat emissions and transportation heat emissions in this study. AHE used in the URB scenario were estimated using the AH4GUC methodology developed by Dong et al. (2017) and Varquez et al. (2021). The AH4GUC approach provides a 1 km resolution AHE dataset derived from LandScan population data (Lebakula et al., 2025), VIIRS nighttime light observations, and regional energy statistics. In this study, the AHE dataset was updated using population and energy consumption statistics for 2022. Because seasonal variations in AHEs are generally small in tropical regions (e.g., Blunn et al., 2024), the same annual-mean AHE dataset was applied to both monsoon seasons. The spatially distributed AHE fields included prescribed diurnal variations and were incorporated into the modified WRF-UCM framework as external inputs. The AHE fields were directly prescribed as a heat source in the lowest atmospheric layer of WRF.

Table 2
The urban surface parameters used in this study were adapted from Morris et al. (2016). Urban category 31 represents low-intensity residential areas, category 32 corresponds to high-intensity residential areas, and category 33 represents commercial or industrial zones.

Urban surface parameters			
Parameters	Urban Category		
	31	32	33
Mean building height (m)	8	12.5	14
Standard deviation of building height (m)	1	4	5
Building roof width (m)	9	11	11
Road width (m)	5	14	21
Heat capacity of roof (MJ $m^{-3}K^{-1}$)	1.20	1.20	1.20
Heat capacity of building wall (MJ $m^{-3}K^{-1}$)	1.40	1.40	1.40
Heat capacity of ground -road (MJ $m^{-3}K^{-1}$)	1.68	1.68	1.68
Thermal conductivity of roof (W $m^{-1}K^{-1}$)	0.67	0.67	0.67
Thermal conductivity of building wall (W $m^{-1}K^{-1}$)	0.80	0.80	0.80
Thermal conductivity of ground -road (W $m^{-1}K^{-1}$)	1.32	1.32	1.32
Surface albedo of roof	0.20	0.20	0.20
Surface albedo of building wall	0.20	0.20	0.20
Surface albedo of ground -road	0.11	0.11	0.11
Surface emissivity of roof	0.90	0.90	0.90
Surface emissivity of building wall	0.90	0.90	0.90
Surface emissivity of ground -road	0.93	0.93	0.93

Table 3
Land use classification conversion from JAXA to weather research and forecasting model (USGS).

JAXA	WRF (USGS)
Water	Water Bodies
Built-up	Urban and Built-Up Land
Solar Panel	Barren or Sparsely Vegetated
Cropland	Mixed Dryland/Irrigated Cropland and Pasture
Single-crop Paddy Field	Irrigated Cropland and Pasture
Multi-crop Paddy Field	Irrigated Cropland and Pasture
Herbaceous Wetland	Herbaceous Wetland
Grassland	Grassland
DBF: Deciduous Broad-leaved Forest	Deciduous Broadleaf Forest
EBF: Evergreen Broad-leaved Forest	Evergreen Broadleaf Forest
ENF: Evergreen Needle-leaved Forest	Evergreen Needleleaf Forest
Rubber Tree Plantation	Cropland/Woodland Mosaic
Oil Palm Tree Plantation	Cropland/Woodland Mosaic
Mangrove Forest	Wooded Wetland
Bare	Barren or Sparsely Vegetated

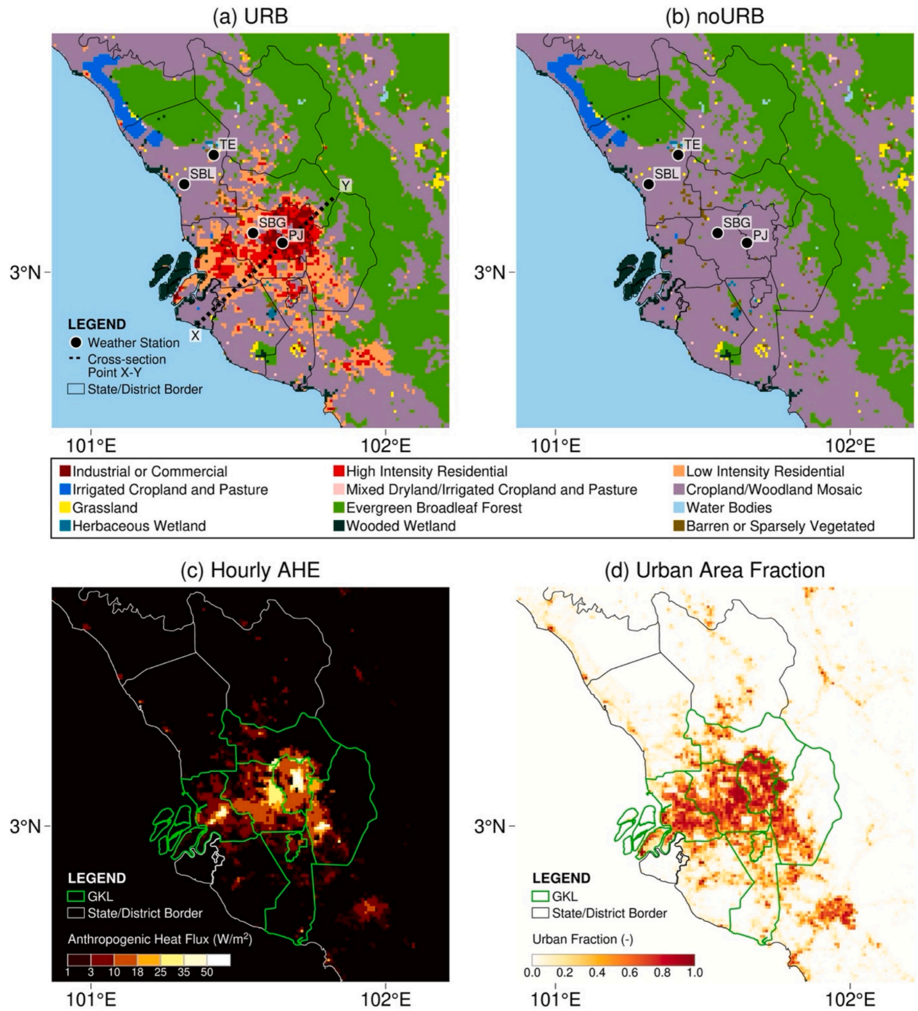

Fig. 3. Maps of JAXA HRLULC-SEA land-use classification for the innermost domain (D03) in the WRF model. (a) Land use map for URB case. The dotted line represents cross-section points (X–Y) used for vertical transect analysis. (b) Land use map for noURB case, where urban areas are replaced with rural land covers, predominantly Cropland/Woodland Mosaic. (c) Spatial distribution of hourly Anthropogenic Heat Flux (AHE) average over the analysis period. (d) Urban fraction distribution over the GKL. The PJ stations is classified as urban-high intensity residential, SGB as urban-low intensity residential, and SBL and TE as Cropland/Woodland Mosaic.

Table 4
The differences between the URB and noURB settings.

Aspect	URB setting	noURB setting
Land use (LU) categories	LU is modified to represent urban land use: categories 31 (low-intensity residential areas), 32 (high-intensity residential areas), and 33 (commercial or industrial zones).	LU is modified to represent rural environments: category 6 (Cropland/Woodland Mosaic).
Anthropogenic Heat Emissions (AHE), W/m^2	Spatially distributed AHE data (see Fig. 3) according to the urban land use categories is derived from population density datasets, energy consumption, traffic emissions, and others (Dong et al., 2017; Varquez et al., 2021).	AHE set to 0, as there are no anthropogenic contributions in rural environments.
Urban fraction	Spatially distributed Urban Area Fraction (see Fig. 3c) according to the urban land use categories	No urban fraction applied, as the grid cells represent entirely rural areas.
Urban parameters	Urban-specific parameters (e.g., building heights, thermal properties as listed in Table 3) included through URBPARM.TBL.	No urban parameters applied, as the rural setting assumes no urban infrastructure.

2.4. Diagnostic methods

2.4.1. Model validation metrics

To evaluate the performance of the WRF model, three standard statistical metrics were calculated for 2 m air temperature (T2) and 2 m relative humidity (RH): mean bias error (MBE), mean absolute error (MAE), and root mean square error (RMSE). Pearson's correlation coefficient (r) and the coefficient of determination (r^2) were also computed to assess the strength of the linear relationship and the overall agreement between simulations and observations.

Model performance was evaluated using hourly surface meteorological observations from four weather stations operated by the Malaysian Meteorological Department (MET Malaysia). To assess model performance under different land-use conditions, the stations were grouped into urban and rural categories. Petaling Jaya (PJ) and Subang (SBG) were classified as urban stations, representing the densely built-up environments within Greater Kuala Lumpur (GKL), whereas Sg. Buloh (SBL), and Tennamaran Estate (TE) were classified as rural stations, representing the surrounding rural and agricultural environments.

2.4.2. Urban cloud island intensity

To quantify the impact of urbanisation on cloud occurrence, this study defines the urban cloud island intensity (UCII) as the difference in cloud occurrence frequency between the URB and noURB simulations:

$$UCII = CF_{URB} - CF_{noURB}$$

where CF denotes cloud occurrence frequency at each grid cell. In this analysis, CF was derived from the column cloud fraction, which was calculated from the three-dimensional cloud fraction diagnosed using the scheme of Xu and Randall (1996). The three-dimensional cloud fraction was first converted to a column cloud fraction based on the random-overlap assumption:

$$C_{\mathrm{col}} = 1 - \prod_{k=1}^{N} (1 - C_k)$$

where C_{col} is the column cloud fraction, C_k is the cloud fraction at the k-th model layer, and N is the total number of model layers. A grid cell was classified as cloudy when $C_{\mathrm{col}} \geq 0.2$ at a given output time. Cloud occurrence frequency, CF, was then calculated as the percentage of cloudy samples relative to the total number of samples within the analysis period and time window.

Positive UCII values indicate an increase in cloud occurrence frequency associated with urbanisation, whereas negative values indicate a decrease.

2.4.3. Moisture transport analysis

To examine the role of moisture transport in urban cloud formation, the vertically integrated horizontal moisture flux was calculated from the WRF outputs. The horizontal moisture flux $\overrightarrow{F_q}$ is defined as the product of specific humidity and the horizontal wind vector (Athar and Ammar, 2015; Cuckow et al., 2022).

To quantify moisture transport within the atmospheric boundary layer, the flux was vertically integrated from the surface to 1000 m above ground level (AGL):

$$\overrightarrow{F_q} = \int_{z=0}^{z=1000m} \rho(z)\, q(z)\, \overrightarrow{V}(z)\, dz$$

where $\rho(z)$ is the air density (kg/m^3), $q(z)$ is the specific humidity (kg/kg), $\overrightarrow{V}(z)$ is the horizontal wind vector (m/s). The units of $\overrightarrow{F_q}$ are $kg\, m^{-1} s^{-1}$, representing the rate of moisture transport per unit area.

This formulation is based on the vertically integrated moisture flux approach of Peixóto and Oort (1992), in which moisture transport is integrated through a vertical atmospheric column (Athar and Ammar, 2015; Scian et al., 2006). In contrast to studies that analyse moisture transport at individual pressure levels, the present approach quantifies the total moisture transport within the lower atmosphere, where urban influences are most pronounced. Moisture flux convergence (MFC, $kg\, m^{-2} s^{-1}$) was also analysed. MFC is a widely used indicator in studies of cloud initiation, convective development, and precipitation patterns (e.g., Kusaka et al., 2014, 2019).

3. Results

3.1. Model validation

The results of the model validation are presented in Table 5, and the corresponding diurnal profiles are shown in Fig. 4. For T2, the model underestimated temperatures, particularly during the daytime (13:00–15:00 LT), but successfully reproduced the observed diurnal variations for both DJF and JJA, as well as the differences between urban and rural environments. In DJF, the bias was −0.9 °C in both urban and rural areas, while the correlation coefficients (r) were 0.90 and 0.94, respectively. In JJA, the bias was −0.2 °C in urban areas and −0.4 °C in rural areas, while the corresponding r values were 0.88 and 0.94, respectively. These statistics indicate good model performance, with accuracy comparable to that reported in previous studies conducted in Malaysian cities (e.g., Morris et al., 2016; Ooi et al., 2017) and U.S. cities (e.g., Moraglia et al., 2024; Moraglia and Crippa, 2026).

For RH, the model overestimated daytime values but effectively reproduced the observed diurnal variations. The bias remained below 10%, while the correlation coefficients ranged from 0.86 to 0.90 during DJF and from 0.73 to 0.84 during JJA. In addition, although the model slightly overestimated the 10-m wind speed, it successfully captured the diurnal variations in both urban and rural environments during both seasons. The wind speed bias was comparable between urban and rural areas, with values of approximately 0.9 m s^{-1} during DJF and 1.1 m s^{-1} during JJA.

The high frequency of daytime cloud occurrences over GKL on hot days was demonstrated in the analysis of Himawari satellite cloud imagery by Syed Mahbar and Kusaka (2024a). A similar trend was reproduced in the URB simulations of this study. For example, during DJF, the frequency of daytime cloud occurrences over GKL was, on average, 8% higher than over the surrounding rural areas and 5% higher compared to JJA.

3.2. Urban-rural thermal contrast

Fig. 5 shows the distribution of urban heat island intensity (UHII), calculated as the difference between the URB and noURB simulations. During DJF, UHII is evident from 11:00 to 19:00 LT and gradually strengthens throughout the day. The centre of the UHII is located over the inland urban area of KL, whereas the UHII is relatively weak near the coast because of the cooling influence of the sea breeze. A similar spatiotemporal evolution is observed during JJA, but the UHII is weaker until 17:00 LT. These results indicate a clear diurnal cycle and spatial pattern of UHII in both seasons.

The observed spatial pattern may be associated with seasonal differences in sea-breeze and monsoonal circulations. During DJF, the sea breeze is weak or absent during the late morning, allowing positive UHII to develop across most of the urban area. As the sea breeze penetrates inland during the afternoon, the urban–rural temperature contrast decreases near the coast because of the cooling influence of marine air. In contrast, the inland urban area remains relatively warm, resulting in a more pronounced UHII over inland KL. During JJA, however, the region is under the persistent influence of the southwest monsoon throughout the day. As a result, the coastal urban area is continuously affected by the advection of relatively cool marine air, which suppresses UHII near the coast and contributes to the weaker daytime UHII, particularly before 17:00 LT, compared with DJF.

3.3. Cloud frequency

To assess the impact of urbanisation on cloud development, Fig. 6 shows the spatial distribution of cloud occurrence frequency differences between the URB and noURB simulations. This difference is referred to as the urban cloud island intensity (UCII), which

Table 5
Model validation results for 2 m temperature (T2, °C) and 2 m relative humidity (RH, %). For validation, data from Petaling Jaya (PJ) and Subang (SBG) stations were used to represent urban areas, while data from Sg. Buloh (SBL), and Tennamaran Estate (TE) stations were used to represent rural areas. The availability of datasets during the study period served as the basis for selecting these stations. The bias assessment compares the observed dataset with the model simulation outputs, averaged across both urban and rural land-use categories.

Season	Category	Variable	MBE	MAE	RMSE	r	r^2
DJF	Urban	T2	−0.9	1.3	1.6	0.9	0.82
		RH	0.3	6.2	7.9	0.86	0.74
		WS	0.9	1.1	1.3	0.51	0.26
	Rural	T2	−0.9	1.2	1.4	0.94	0.88
		RH	1.0	4.9	6.2	0.9	0.82
		WS	0.9	1.0	1.2	0.55	0.31
JJA	Urban	T2	−0.2	1.0	1.3	0.88	0.77
		RH	−1.0	7.4	9.2	0.73	0.53
		WS	0.8	1.0	1.2	0.69	0.47
	Rural	T2	−0.4	1.0	1.2	0.94	0.89
		RH	−1.3	6.3	7.8	0.84	0.7
		WS	1.1	1.1	1.3	0.71	0.5

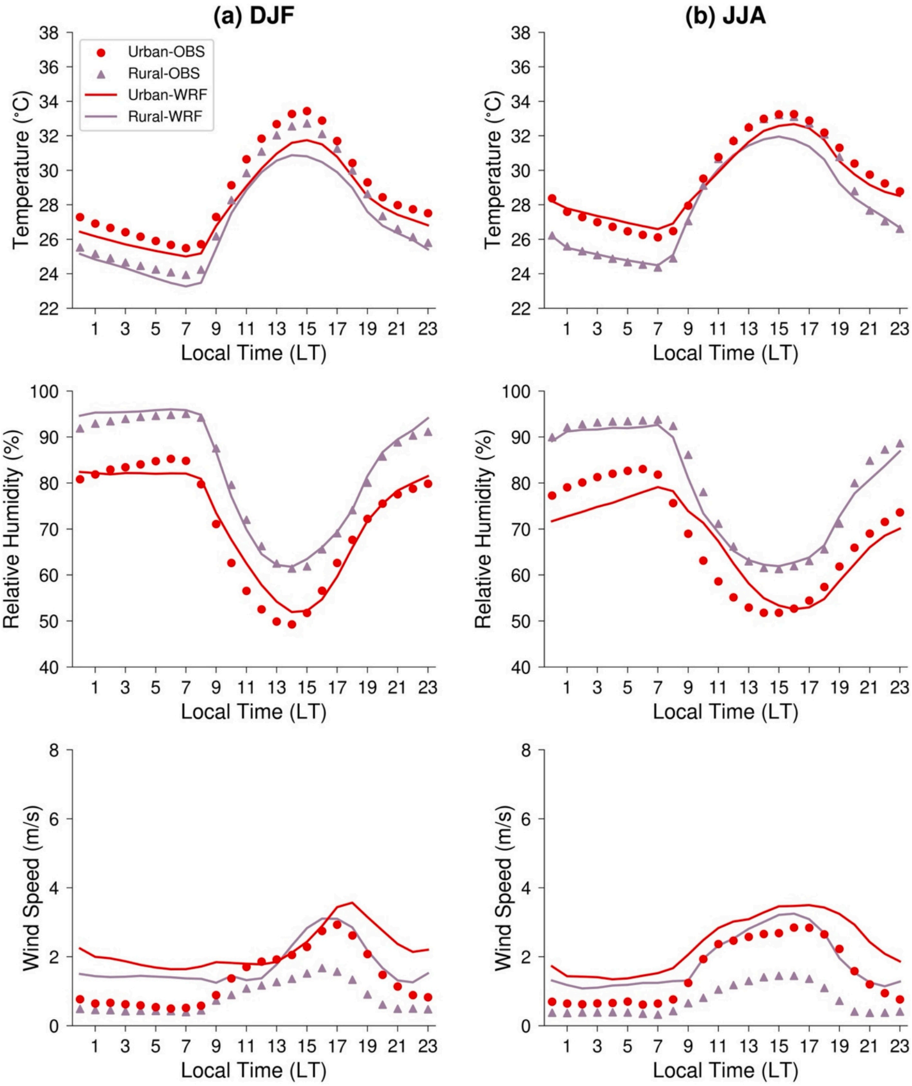

Fig. 4. Diurnal profiles of 2 m temperature (T2), 2 m relative humidity (RH), and 10 m wind speed (WSPD) for urban and rural categories during hot-day cases. Results are shown separately for DJF and JJA. Red colours represent the urban category, and purple colours represent the rural category. The scatter plots represent observational data, while the line plots represent model simulations. (For interpretation of the references to colour in this figure legend, the reader is referred to the web version of this article.)

represents the extent to which urbanisation enhances or suppresses cloud formation relative to the surrounding rural areas.

During DJF, enhanced cloud development is evident over the urban core as early as 14:00–16:00 LT. Positive CF differences are found across the entire urban area, exceeding 3% in most locations. The largest increase occurs around the PJ area, where the CF difference exceeds 18%. The spatial distribution of UCII closely corresponds to the urbanised area, indicating a positive UCII signal over GKL. This feature persists until 19:00 LT and becomes more pronounced with time. In JJA, positive UCII values are primarily confined to the inland (downwind) side of the urban area. Compared with DJF, the UCII signal is weaker, covers a smaller area, and exhibits less pronounced diurnal variability. The contrasting diurnal evolution of UCII between DJF and JJA is also reflected in the temporal variation of the urban area-averaged UCII (Fig. 7).

3.4. *Surface heat fluxes*

Sensible heat flux (SH) serves as a direct indicator of surface heating and plays an important role in controlling atmospheric stability and boundary-layer development. In urban environments, SH is strongly influenced by impervious surfaces, reduced vegetation cover, and anthropogenic heat emissions, all of which enhance surface warming. As shown in Fig. 8, urban areas in GKL consistently exhibit higher SH than the surrounding rural areas. The maximum simulated SH in urban areas is approximately 1.4 times greater than that in rural areas during both JJA and DJF, reflecting the enhanced surface heating associated with urbanisation. The

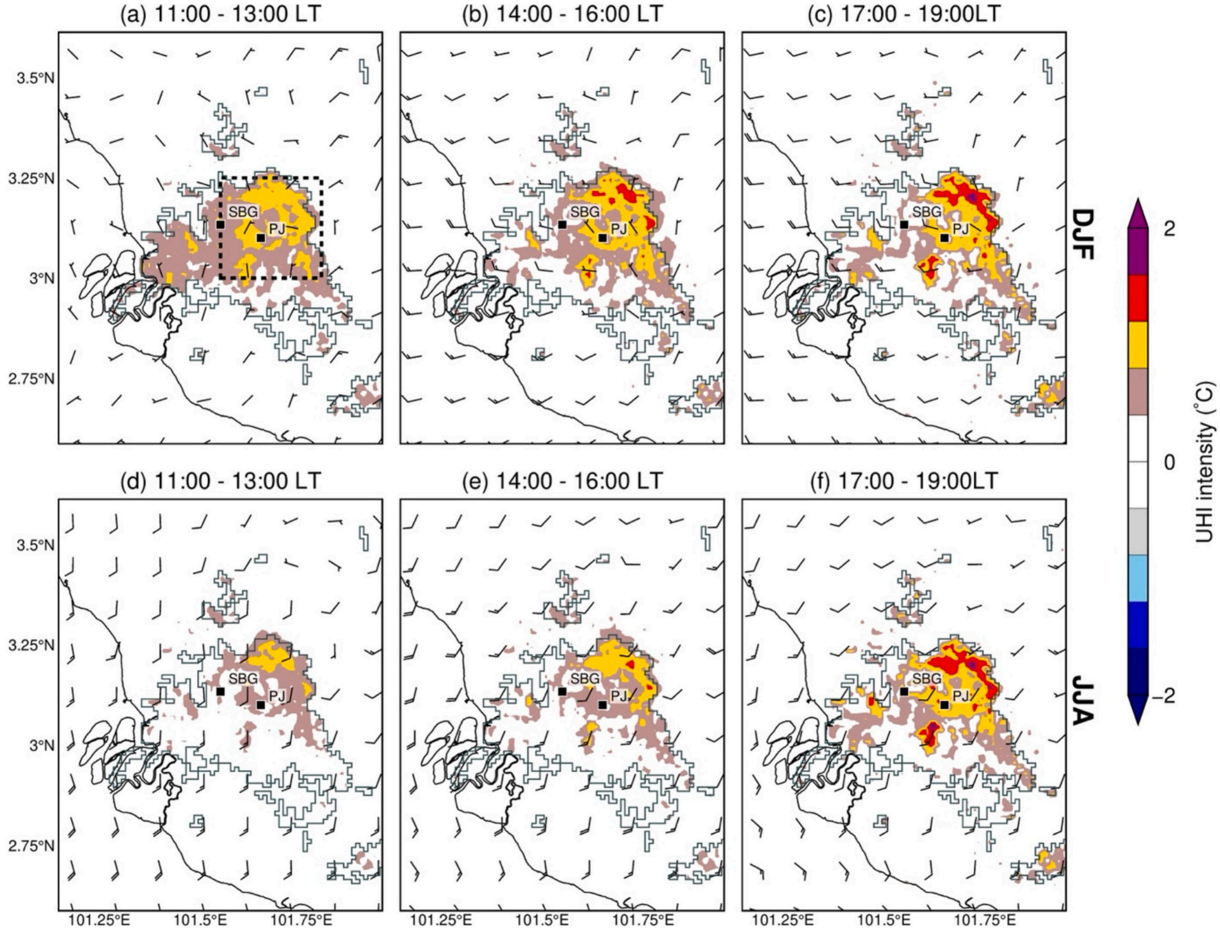

Fig. 5. Urban heat island (UHI) intensity (°C) during DJF (top) and JJA (bottom), derived from the simulations (URB − noURB). Panels (a), (b), and (c) show the mean UHI distribution during 11:00–13:00 LT, 14:00–16:00 LT, and 17:00–19:00 LT, respectively, for DJF, while panels (d), (e), and (f) show the corresponding distributions for JJA. The 10 m wind vectors are overlaid, and the locations of the sites of interest (TE, SBL, JA, SBG, and PJ) are indicated for reference. Shaded colours represent UHI intensity, with warm colours indicating positive values and cool colours indicating negative values.

diurnal evolution of SH is similar in both seasons, increasing rapidly after sunrise, peaking between 13:00 and 15:00 LT, and gradually decreasing toward the evening. In contrast, latent heat flux (LH) is consistently lower in urban areas and higher in rural areas, reflecting the reduced evapotranspiration associated with urban land cover.

3.5. Boundary layer dynamics and moisture availability

Fig. 9 illustrates the diurnal evolution of planetary boundary layer height (PBLH) and lifting condensation level (LCL) over the central urban area. During DJF, the boundary layer in the URB simulation is consistently deeper than that in the noURB simulation owing to enhanced surface heating. The difference in PBLH reaches approximately 260 m at 15:00 LT. Urbanisation also increases the LCL by 200 m at 15:00 LT because the URB simulation exhibits higher air temperatures and lower relative humidity than the noURB simulation (Fig. 10). These results suggest that the enhanced boundary-layer development associated with urbanisation largely offsets the negative effect of elevated LCL on cloud formation. A similar relationship is observed during JJA; however, the urban-induced increases in both PBLH and LCL are smaller than those during DJF.

Fig. 11 shows the impact of urbanisation on water vapour mixing ratio in a vertical cross-section. The water vapour mixing ratio in the URB simulation exceeds that in the noURB simulation, with the largest differences occurring between approximately 1200 and 2500 m in DJF across the urbanised region. The maximum increase occurs near 2400 m altitude over the inland urban area adjacent to the mountain, reaching up to 1.8 g kg^{-1} in the URB simulation relative to the noURB simulation. This pattern suggests that moisture advection from surrounding rural areas and adjacent oceans increases atmospheric moisture content within and above the boundary layer, despite the lower surface latent heat flux in the URB simulation than in the noURB simulation. In JJA, the maximum increase occurs at lower altitudes and is confined to the inland urban area and the adjacent mountain slope.

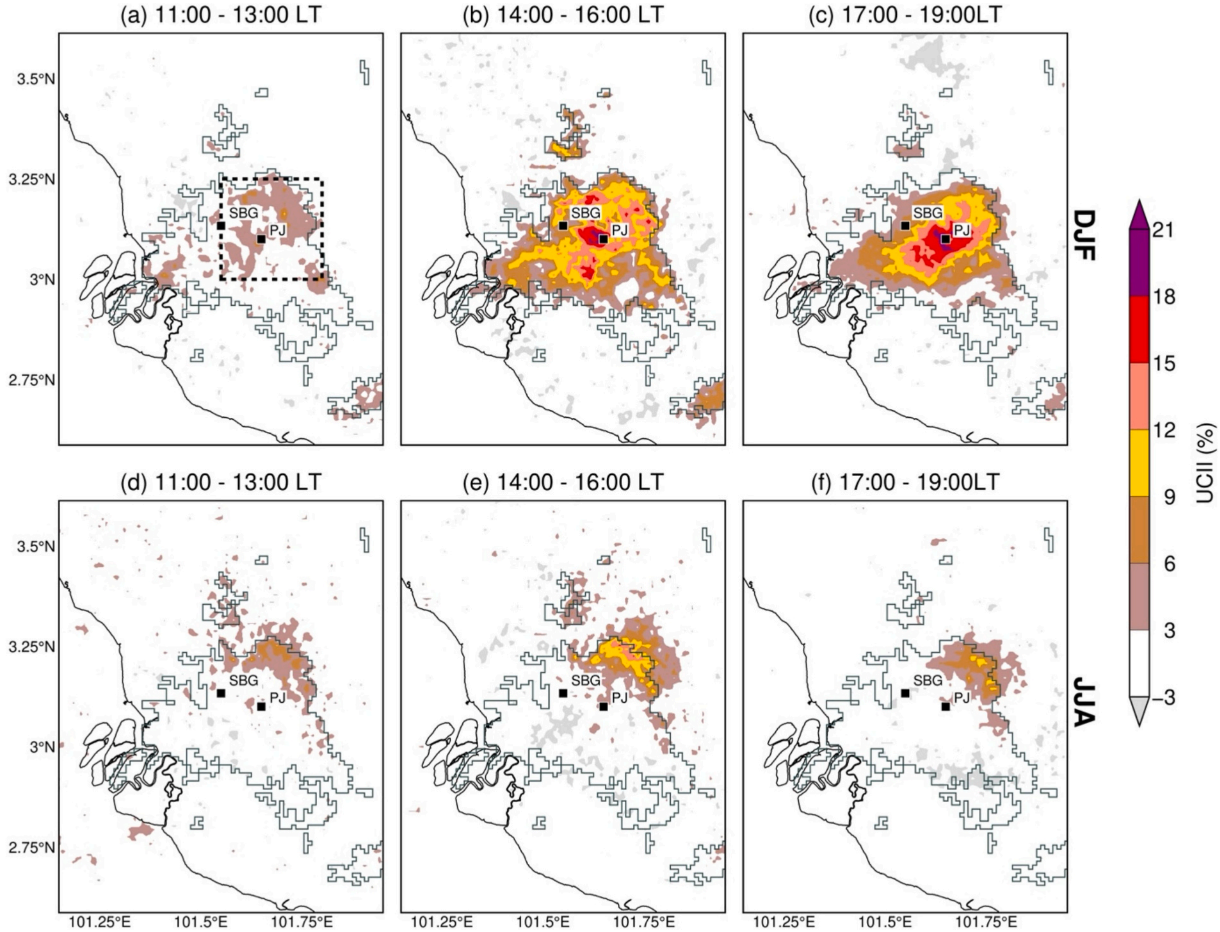

Fig. 6. Cloud occurrence frequency contrast between the URB and noURB simulations, defined as urban cloud island intensity (UCII), for DJF (top) and JJA (bottom) during (a) 11:00–13:00 LT, (b) 14:00–16:00 LT, and (c) 17:00–19:00 LT, illustrating the progression of cloud development over the urbanised GKL region. Red to magenta tones highlight higher values of cloud frequency contrast, brown to yellow tones represent moderate contrast, white indicates small differences, and grey tones indicate negative differences. (For interpretation of the references to colour in this figure legend, the reader is referred to the web version of this article.)

3.6. Moisture transport

Fig. 12 shows the vertically integrated moisture flux and moisture flux convergence (MFC) during the convective afternoon period (13:00–17:00 LT) for DJF and JJA. The corresponding differences between the URB and noURB simulations (URB − noURB) are also presented. In DJF, the vertically integrated moisture flux vectors in the URB simulation indicate that moisture transported from the ocean and the surrounding mountainous region converges over the urban area (Fig. 12a). The difference between the URB and noURB simulations shows that urbanisation enhances moisture transport toward GKL and increases moisture convergence across the urban region (Fig. 12b). These results suggest that urbanisation strengthens both the sea-breeze circulation and the urban heat island (UHI)-induced circulation over the region, leading to enhanced moisture flux convergence. The areas of enhanced MFC correspond closely to the areas of increased cloud occurrence frequency, supporting the hypothesis that enhanced moisture convergence contributes to increased cloud occurrence over GKL. In JJA, moisture is transported primarily from the south (Fig. 12c). Urbanisation slightly enhances moisture transport from the southwest (Fig. 12d). The increase in moisture convergence is mainly confined to the inland urban area. As in DJF, the regions of enhanced MFC correspond closely to the regions of increased cloud occurrence frequency. These results indicate that urbanisation-induced changes in moisture transport also contribute to enhanced cloud occurrence frequency during JJA.

This seasonal difference is likely a result of seasonal changes in monsoonal wind direction (Fig. S1), which modify the interaction of sea-breeze and urban heat island circulations and consequently alter the location and spatial extent of moisture convergence. These results suggest that urbanisation modifies the interaction between the background monsoonal flow, sea-breeze circulation, and UHI circulation, thereby altering the location and intensity of moisture convergence and the associated cloud response.

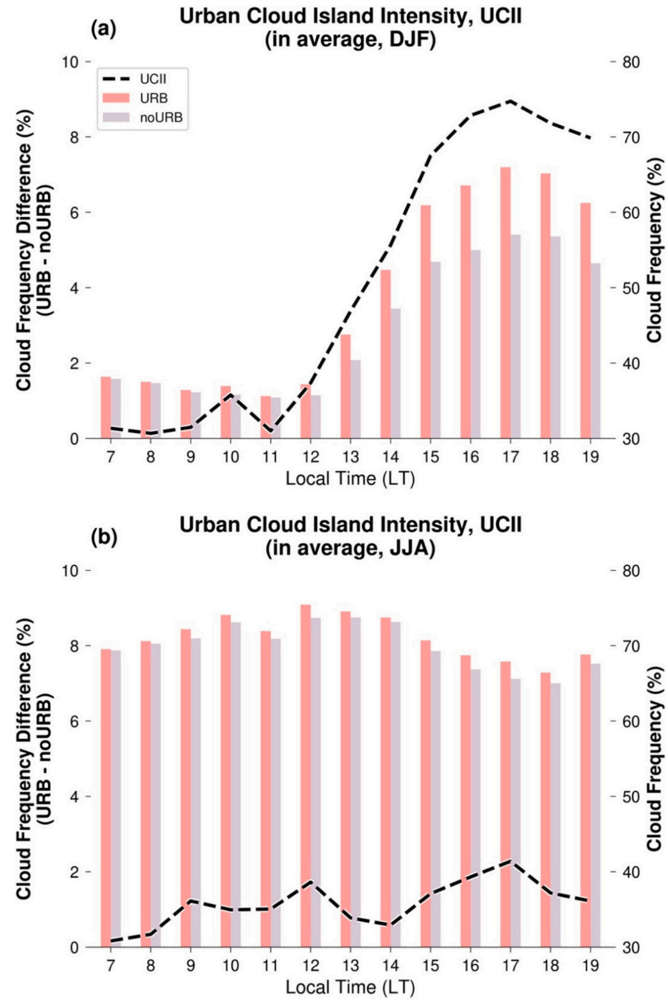

Fig. 7. Time series of urban cloud island intensity (UCII) during (a) DJF and (b) JJA, averaged over all cases within the region enclosed by the black dotted line in Fig. 6(a). The dashed black lines denote the UCII derived from the URB − noURB simulations. The bars show the regional mean cloud frequency (CF), with red and purple shades representing results from the URB and noURB experiments, respectively. (For interpretation of the references to colour in this figure legend, the reader is referred to the web version of this article.)

4. Discussion

Our study demonstrated that urbanisation leads to greater boundary-layer development over urban areas than over surrounding rural areas. This result is consistent with the findings of Kang and Bryan (2011) and Moriwaki et al. (2013), who reported higher cloud-base heights and planetary boundary-layer heights (PBLH) over warmer surfaces. The enhanced boundary-layer growth found in this study promotes the upward transport of moisture and increases the likelihood of cloud formation over urban areas.

Previous studies have shown that urban-induced thermal forcing can modify local circulations and moisture transport. Kang and Bryan (2011) and Theeuwes et al. (2022) demonstrated that urban heating generates mesoscale circulations that enhance moisture convergence and cloud development. In particular, Theeuwes et al. (2022) showed that UHI-induced circulations, together with sea-breeze effects, transport moisture from surrounding areas toward the urban centre, resulting in enhanced cloud formation. Our study, conducted in Kuala Lumpur, supports these findings. During midday, a sea breeze from the Straits of Malacca interacts with urban heating, contributing to moisture transport toward GKL. Ooi et al. (2017) similarly showed that urban-induced heating intensifies the land–sea breeze circulation, establishing GKL as a convergence zone that attracts moisture-laden air toward the city. The analysis of vertically integrated moisture flux (0–1000 m AGL) in the present study further supports this mechanism, showing enhanced moisture convergence over GKL in the URB simulation relative to the noURB simulation. Together with the increased water vapour mixing ratio over the urban area, these results suggest that urban-induced circulations strengthen moisture convergence and create favourable conditions for cloud formation. Furthermore, our results indicate that these circulations do not operate independently of the large-scale environment. Rather, the sea-breeze and urban heat island circulations are embedded within the prevailing monsoonal flow and are substantially modified by urbanisation. The resulting changes in the interaction among these circulation systems contribute to

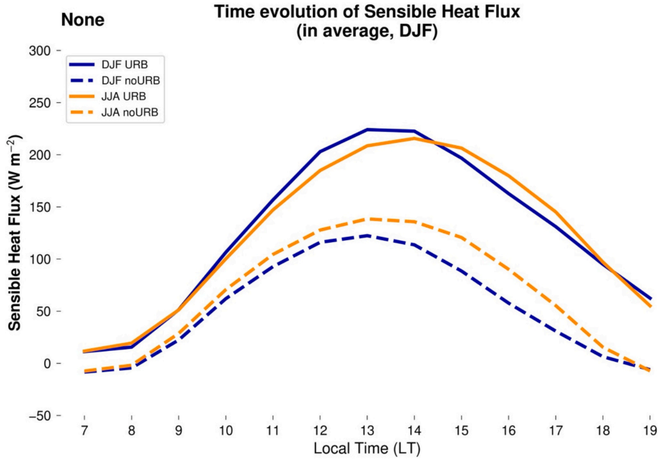

Fig. 8. Diurnal variations of surface sensible heat flux (SH) during DJF and JJA. The values represent area averages over the region enclosed by the black dotted line in Fig. 6(a), composited over all cases. Blue and orange solid lines denote the diurnal variations of SH (W m^{-2}) for the DJF and JJA experiments, respectively. Solid and dashed lines indicate the URB and noURB simulations, respectively. (For interpretation of the references to colour in this figure legend, the reader is referred to the web version of this article.)

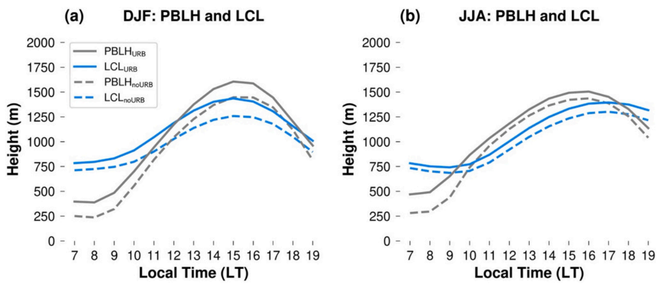

Fig. 9. Diurnal variations of Planetary Boundary Layer Height (PBLH) and Lifting Condensation Level (LCL). Panels (a) and (b) show the composite diurnal variations of PBLH and LCL during DJF and JJA, respectively. The values represent area averages over the region enclosed by the black dotted line in Fig. 6(a), composited over all cases. Dark grey and light blue lines denote PBLH and LCL, respectively, while solid and dashed lines indicate the URB and noURB simulations, respectively. (For interpretation of the references to colour in this figure legend, the reader is referred to the web version of this article.)

the enhanced moisture convergence and cloud formation observed over GKL.

Seasonal differences also emerge in the spatial extent of moisture convergence. During DJF, the convergence field is broader and more spatially continuous, whereas during JJA, enhanced convergence is mainly confined to the inland urban area. These findings provide a physical explanation for the higher cloud occurrence frequency over urban areas reported in the satellite-based statistical analysis of Syed Mahbar and Kusaka (2024a). They further indicate that GKL acts as a regional moisture sink, enhancing local moisture convergence through interactions among the monsoonal flow, sea-breeze circulation, and urban heat island circulation.

Moreover, urban size, urban morphology, geographical setting, surface characteristics, and thermal properties can all influence cloud occurrence (Vo et al., 2023; Quante, 2004; Cui et al., 2026). As Vo et al. (2023) highlighted, larger cities with stronger urban heat islands tend to exhibit enhanced cloud formation owing to stronger thermal gradients and associated moisture transport. Similarly, Quante (2004) emphasised the importance of moisture transport from oceans and other water bodies to inland areas. Our results are consistent with these previous studies.

In recent years, increasing attention has been given to projecting future urban climates. Lin et al. (2008) and Miao et al. (2011) demonstrated that urban expansion can modify precipitation patterns over Taipei and Beijing, respectively, highlighting the importance of urban development in shaping local hydroclimatic conditions. Kusaka et al. (2014) showed that, even when the urban area is held constant, a hypothetical commercial-city scenario generates more convective precipitation than a hypothetical residential-city scenario in the Tokyo metropolitan area. Zhang et al. (2022) further demonstrated that city morphology can significantly affect urban precipitation. These findings suggest that further urban development in GKL may lead to additional increases in cloud occurrence and precipitation.

Prior researches have shown that urban precipitation simulations are often more sensitive to the choice of cloud microphysics parameterisation than to urban area itself (e.g., Zhou et al., 2024). To assess the sensitivity of our results to the choice of microphysics scheme, additional simulations were conducted using the Milbrandt–Yau double-moment microphysics scheme in the present study.

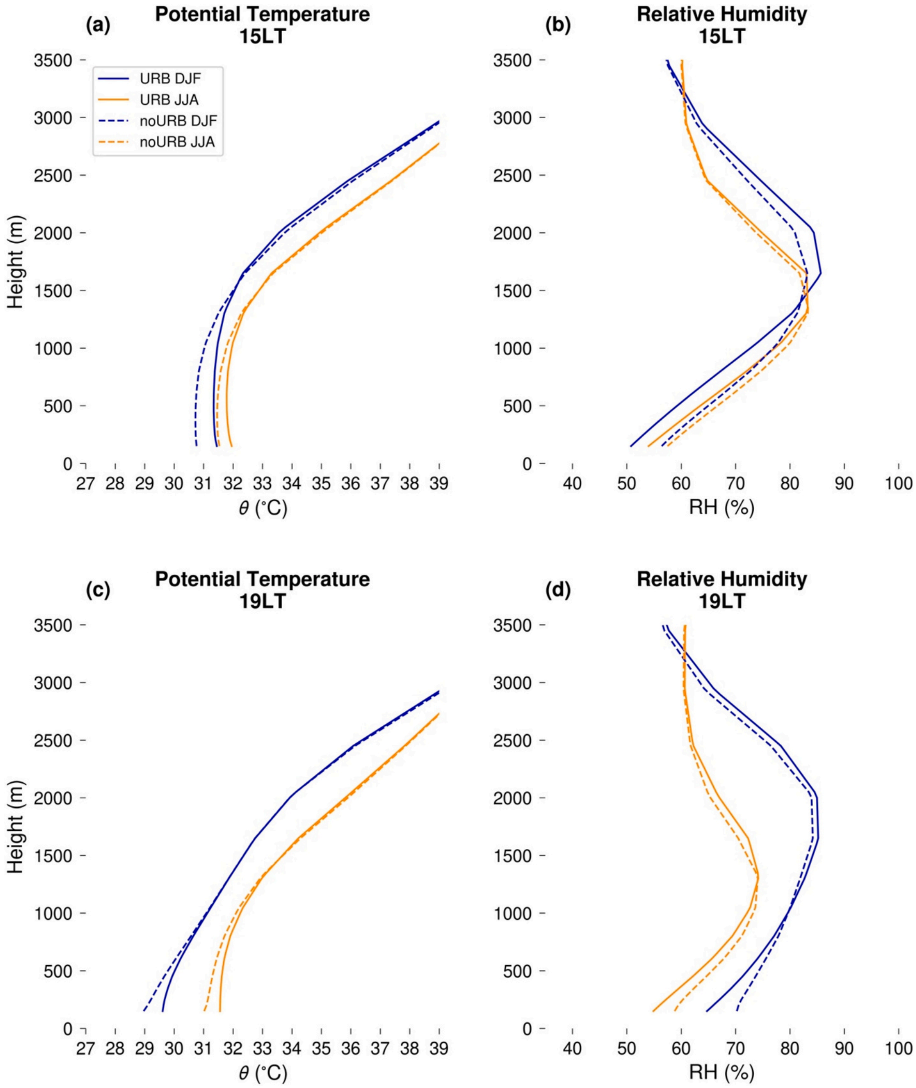

Fig. 10. Vertical profiles of potential temperature and relative humidity in the URB and noURB simulations during DJF and JJA. Panels (a) and (b) show potential temperature and relative humidity at 15:00 LT, respectively, while panels (c) and (d) show potential temperature and relative humidity at 19:00 LT, respectively. The profiles represent area averages over the region enclosed by the black dotted line in Fig. 6(a), composited over all cases. Solid lines denote urban conditions from the URB simulation, whereas dashed lines denote rural conditions from the noURB simulation. Blue and orange lines correspond to DJF and JJA, respectively. (For interpretation of the references to colour in this figure legend, the reader is referred to the web version of this article.)

The impacts of urbanisation on cloud occurrence were generally consistent with those obtained using the Thompson scheme, and no fundamental differences were identified between the two sets of simulations (Fig. 13). One possible explanation is that GKL is located in a tropical coastal environment, where the representation of boundary-layer processes and sea-breeze circulation may play a more important role than the choice of microphysics scheme. Further research is required to better understand the relative importance of these processes.

5. Conclusions

The findings of this study have broader implications for understanding urban cloud formation in densely populated tropical cities such as GKL. Numerical experiments with and without urban areas demonstrate that urbanisation amplifies cloud formation compared with rural surroundings through the combined effects of enhanced sensible heat flux, deeper boundary-layer development, and moisture advection driven by urbanisation-induced modifications of the interaction between the background monsoonal flow, sea-breeze circulation, and urban heat island (UHI) circulation.

Enhanced sensible heat flux from urban areas contributes to a consistently deeper mixed layer over the urban region. Interestingly,

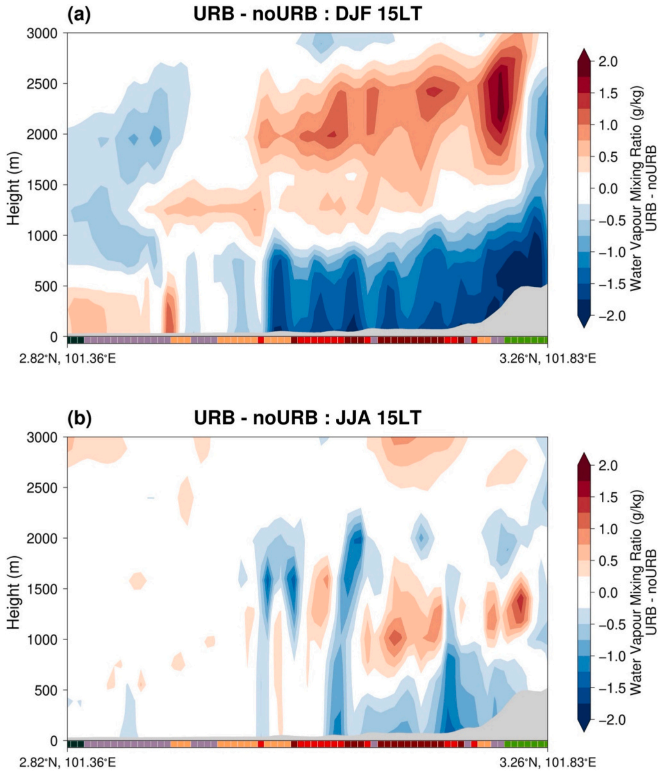

Fig. 11. Vertical cross-sections at 15:00 LT along the X–Y transect shown in Fig. 3. Colours indicate the URB − noURB differences in water vapour mixing ratio, while grey shading denotes terrain. The coloured bands at the bottom of each panel indicate the land-use categories used in the model (see the legend in Fig. 3). Panels (a) and (b) show the results for DJF and JJA, respectively.

despite lower latent heat fluxes and reduced near-surface relative humidity—which would typically raise the lifting condensation level (LCL) and suppress cloud formation—cloud frequency is nevertheless enhanced over GKL. This apparent contradiction points to two distinctive mechanisms that promote cloud development in urban areas. First, the enhanced boundary-layer height associated with urbanisation largely offsets the negative effect of an elevated LCL on cloud formation. Second, UHI and sea-breeze circulations facilitate horizontal moisture advection from surrounding rural areas and the adjacent ocean into the urban area, increasing atmospheric moisture within the urban boundary layer and creating conditions more favourable for cloud development. Our results broadly support previous studies, including Theeuwes et al. (2019, 2022), which demonstrated that urban areas can enhance cloud formation and identified these mechanisms.

The spatial distribution of urban-induced cloud occurrence frequency exhibits a clear seasonal dependence. During the wet season (DJF), urbanisation increases cloud occurrence frequency throughout much of the GKL region. In contrast, during the dry season (JJA), enhanced cloud occurrence frequency is spatially confined to inland urban areas. Areas of enhanced horizontal moisture flux convergence closely correspond to areas of increased cloud occurrence frequency. These findings indicate that urban cloud formation is strongly controlled by moisture convergence within the boundary layer. Furthermore, the seasonal differences suggest that urbanisation modifies the interaction between the background monsoonal flow, sea-breeze circulation, and urban heat island circulation, thereby altering the location and intensity of moisture convergence and the associated cloud response.

Understanding how urban environments intensify cloud formation and alter boundary-layer dynamics is essential for improving the prediction of local weather phenomena, including convective rainfall, cloud-cover variability, and temperature fluctuations, in rapidly developing urban areas. This knowledge also supports urban planning aimed at mitigating heat-related risks, managing urban hydrology, and enhancing resilience to climate extremes.

While this study provides valuable insights, several limitations should be acknowledged. First, the findings are based on a single case study of a tropical conurbation, and further investigations in other tropical cities are needed to assess the broader applicability of the findings. Second, the WRF model underestimated the daily maximum temperature during DJF, suggesting biases in the simulated mean potential temperature and boundary layer height. These biases may be related to uncertainties in the lateral or lower boundary conditions, including errors in the global objective analysis data or an underestimation of the surface sensible heat flux. Third, the present study did not consider the effects of aerosols on cloud formation and precipitation. Aerosol–cloud interactions are known to influence cloud microphysical processes and may modify the impacts of urbanisation on cloud development. Assessing these effects requires additional modelling complexity and therefore warrants dedicated investigation. Further research is needed to quantify the role of aerosols in urban cloud formation over GKL. Despite these limitations, the present study advances our understanding of the

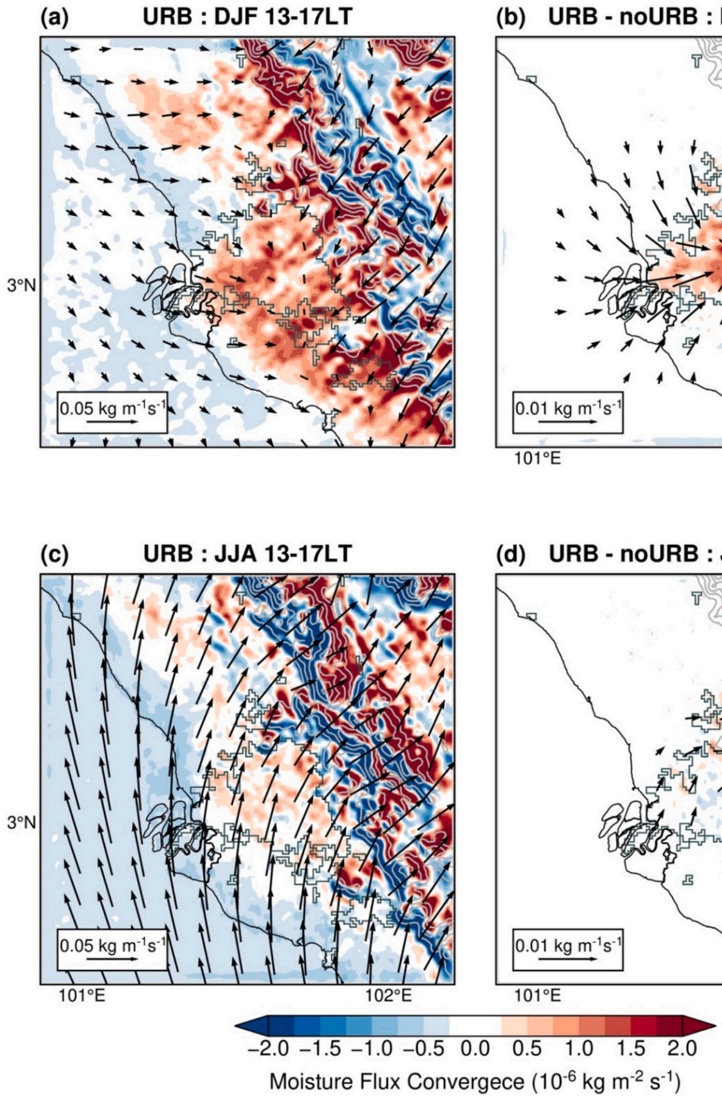

Fig. 12. Vertically integrated horizontal moisture flux and moisture flux convergence (MFC) over the GKL region during the afternoon period (14:00–18:00 LT). Panels (a) and (c) show the moisture flux and MFC from the URB simulation during DJF and JJA, respectively, while panels (b) and (d) show the corresponding URB − noURB differences. Black arrows indicate the vertically integrated horizontal moisture flux, and shaded colours represent MFC. In panels (b) and (d), both quantities are shown as URB − noURB differences. Positive MFC values indicate moisture convergence, whereas negative values indicate moisture divergence. Light grey contour lines denote terrain elevation at 500 m intervals, and black contour lines delineate the urban area.

influence of urbanisation on cloud formation in tropical environments and highlights several important directions for future research.

CRediT authorship contribution statement

Sharifah Faridah Syed Mahbar: Writing – original draft, Visualization, Validation, Software, Methodology, Investigation, Formal analysis, Data curation, Conceptualization. **Nobuyasu Suzuki:** Conceptualization, Data curation, Formal analysis, Investigation, Methodology, Software, Visualization, Writing – review & editing. **Hiroyuki Kusaka:** Writing – review & editing, Writing – original draft, Supervision, Resources, Project administration, Methodology, Funding acquisition, Conceptualization.

Funding information

JSPS KAKENHI Grant Number JP24K07130.

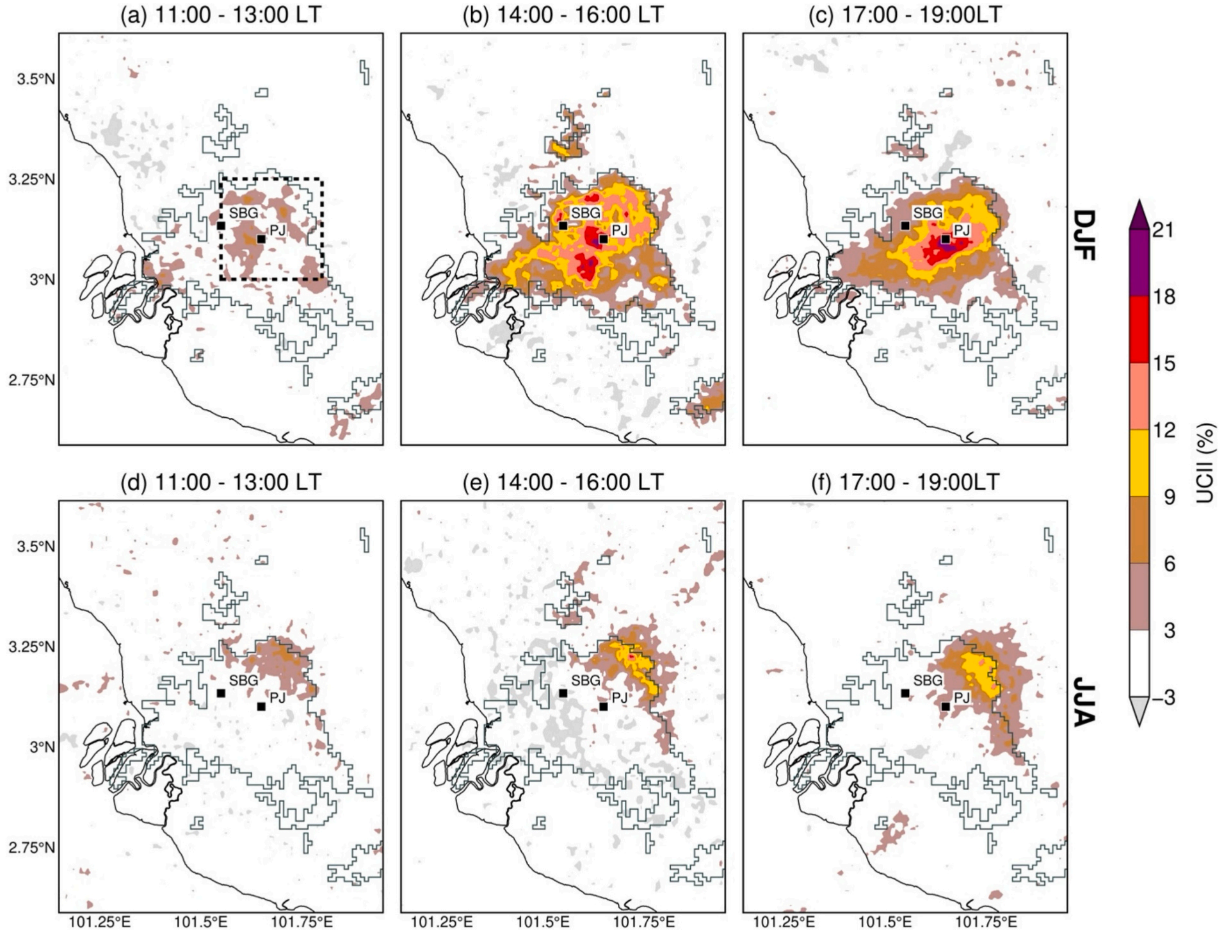

Fig. 13. Same as Fig. 6, but for the sensitivity experiment using the Milbrandt–Yau double-moment microphysics scheme.

Declaration of competing interest

The authors declare that they have no competing financial or non-financial interests that could influence the content or findings of this study.

Acknowledgments

This study was supported by JSPS KAKENHI Grant Number JP24K07130 and partly supported by Multidisciplinary Cooperative Research Program in Center for Computational Sciences, University of Tsukuba. We thank the Malaysian Meteorological Department (MET Malaysia) for providing the observational data used in our statistical analysis and model validation. The first author would like to express her gratitude to the Public Service Department of Malaysia for the scholarships. Land use data were based on high-resolution land-use and land-cover data of Southeast Asia region provided by JAXA's EORC. Himawari 8/9 gridded data are distributed by the Center for Environmental Remote Sensing (CEReS), Chiba University, Japan.

Appendix A. Supplementary data

Supplementary data to this article can be found online at https://doi.org/10.1016/j.uclim.2026.103050.

Data availability

The data utilized in this study is available upon request. Some of the data is subject to the provisions outlined in the Data Act, which preclude their sharing.

References

An, D., Eggeling, J., Zhang, L., He, H., Sapkota, A., Wang, Y.-C., Gao, C., 2023. Extreme precipitation patterns in the Asia-Pacific region and its correlation with El Nino-Southern Oscillation (ENSO). Sci. Rep. 13, 11068. https://doi.org/10.1038/s41598-023-38317-0.

Angevine, W.M., White, A.B., Senff, C.J., Trainer, M., Banta, R.M., Ayoub, M.A., 2003. Urban-rural contrasts in mixing height and cloudiness over Nashville in 1999. J. Geophys. Res. Atmos. 108, 4092. https://doi.org/10.1029/2001jd001061.

Aota, Y., Kusaka, H., 2026. Urban impacts on convective precipitation in the Osaka metropolitan area: numerical simulations over 320 potential precipitation days. J. Appl. Meteorol. Climatol. 65, 323–340. https://doi.org/10.1175/JAMC-D-25-0043.1.

Athar, H., Ammar, K., 2015. Seasonal characteristics of the large-scale moisture flux transport over the Arabian Peninsula. Theor. Appl. Climatol. 124, 565–578. https://doi.org/10.1007/s00704-015-1437-7.

Bhuiyan, T.R., Reza, M.I.H., Choy, E.A., Pereira, J.J., 2018. Facts and trends of urban exposure to flash flood: a case of Kuala Lumpur City. In: Improving Flood Management, Prediction and Monitoring-Community, Environment and Disaster Risk Management, 20, pp. 79–90. https://doi.org/10.1108/S2040-726220180000020016.

Blunn, L., et al., 2024. Spatial and temporal variation of anthropogenic heat emissions in Colombo, Sri Lanka. Urban Clim. 54, 101828. https://doi.org/10.1016/j.uclim.2024.101828.

Chen, F., et al., 2011. The integrated WRF/urban modeling system: development, evaluation, and applications to urban environmental problems. Int. J. Climatol. 31, 273–288. https://doi.org/10.1002/joc.2158.

Chew, L.W., Liu, X., Li, X.-X., Norford, L.K., 2020. Interaction between heat wave and urban heat island: a case study in a tropical coastal city, Singapore. Atmos. Res. 247, 105134. https://doi.org/10.1016/j.atmosres.2020.105134.

Cuckow, S., Dacre, H.F., Oscar, M.-A., 2022. Moisture transport contributing to precipitation at the Centre of storm Bronagh. Weather 77, 196–201. https://doi.org/10.1002/wea.4212.

Cui, Y., Chen, S., Xue, L., Munoz-Esparza, D., Sauer, J.A., Hu, L., Albertson, J.D., Li, Q., 2026. Local cloud enhancement associated with urban morphology: evidence from observations and idealized large-eddy simulations. Nat. Commun. 17, 2378. https://doi.org/10.1038/s41467-026-68986-0.

Danchovski, A., 2024. Impact of urbanisation on cloud characteristics over Sofia, Bulgaria. Remote Sens. 16, 1631. https://doi.org/10.3390/rs16091631.

Doan, Q.-V., Kusaka, H., 2018. Projections of urban climate in the 2050s in a fast-growing city in Southeast Asia: the greater Ho Chi Minh City metropolitan area, Vietnam. Int. J. Climatol. 38, 4155–4171. https://doi.org/10.1002/joc.5559.

Doan, Q.-V., Kusaka, H., Nguyen, T.M., 2019. Roles of past, present, and future land use and anthropogenic heat release changes on urban heat island effects in Hanoi, Vietnam: numerical experiments with a regional climate model. Sustain. Cities Soc. 47, 101479. https://doi.org/10.1016/j.scs.2019.101479.

Doan, Q.-V., Dipankar, A., Simón-Moral, A., Sanchez, C., Prasanna, V., Roth, M., Huang, X.-Y., 2021. Urban-induced modifications to the diurnal cycle of rainfall over a tropical city. Q. J. R. Meteorol. Soc. 147, 1189–1201. https://doi.org/10.1002/qj.3966.

Dong, Y., Varquez, A.C.G., Kanda, M., 2017. Global anthropogenic heat flux database with high spatial resolution. Atmos. Environ. 150, 276–294. https://doi.org/10.1016/j.atmosenv.2016.11.040.

Dudhia, J., 1989. Numerical study of convection observed during the Winter Monsoon Experiment using a mesoscale two–dimensional model. J. Atmos. Sci. 46, 3077–3107. https://doi.org/10.1175/1520-0469(1989)046<3077:NSOCOD>2.0.CO;2.

Fujibe, F., Togawa, H., Sakata, M., 2009. Long-term change and spatial anomaly of warm season afternoon precipitation in Tokyo. SOLA 5, 17–20. https://doi.org/10.2151/sola.2009-005.

Gettelman, A., Sherwood, S.C., 2016. Processes responsible for cloud feedback. Curr. Clim. Chang. Rep. 2, 179–189. https://doi.org/10.1007/s40641-016-0052-8.

Ghielmini, C., Pausata, F.S.R., Argueso, D., et al., 2024. Evaluating the role of city representation in modelling the urban precipitation effect of Kuala Lumpur. Urban Clim. 55, 101907. https://doi.org/10.1016/j.uclim.2024.101907.

Han, J.-Y., Baik, J.-J., Lee, H., 2014. Urban impacts on precipitation. Asia-Pac. J. Atmos. Sci. 50, 17–30. https://doi.org/10.1007/s13143-014-0016-7.

Hasebe, S., Kusaka, H., Suzuki, N., Thanh, N.-D., 2026. Urban impacts on precipitation in the Greater Ho Chi Minh City Metropolitan Area, Vietnam. J. Geophys. Res.-Atmos. 131, e2025JD045001. https://doi.org/10.1029/2025JD045001.

Huang, B., et al., 2021. Improvements of daily optimum interpolation sea surface temperature (DOISST) version 2.1. J. Clim. 34, 2923–2939. https://doi.org/10.1175/JCLI-D-20-0166.1.

Inoue, T., Kimura, F., 2007. Numerical experiments on fair-weather clouds forming over the urban area in northern Tokyo. SOLA 3, 125–128. https://doi.org/10.2151/sola.2007-032.

IPCC, 2021. AR6 Climate Change 2021: The Physical Science Basis. Contribution of Working Group I to the Sixth Assessment Report of the Intergovernmental Panel on Climate Change. Cambridge University Press.

Jamaluddin, A.F., Tangang, F., Cung, J.X., Juneng, L., Sasaki, H., Takayabu, I., 2018. Investigating the mechanism of diurnal rainfall variability over Peninsular Malaysia using the non-hydrostatic regional climate model. Meteorog. Atmos. Phys. 130, 611–633. https://doi.org/10.1007/s00703-017-0541-x.

Jamaluddin, A.F., Mustafa Kamal, M.I., Abdullah, M.H., Marodzi, A.N., 2022. Comparison between satellite-derived rainfall and rain gauge observation over Peninsular Malaysia. Sains Malaysiana 51, 67–81. https://doi.org/10.17576/jsm-2022-5101-06.

Jankov, I., Gallus Jr., W.A., Segal, M., Shaw, B., Koch, S.E., 2005. The impact of different WRF model physical parameterizations and their interactions on warm season MCS rainfall. Weather Forecast. 20, 1048–1060. https://doi.org/10.1175/WAF888.1.

Kanda, M., Inoue, Y., Uno, I., 2001. Numerical study on cloud lines over an urban street in Tokyo. Bound.-Layer Meteorol. 98, 251–273. Kluwer Academic Publisher.

Kang, S.-L., Bryan, G.H., 2011. A Larg-Eddy simulation study of moist convection initiation over heterogeneous surface fluxes. Mon. Weather Rev. 139, 2901–2917. https://doi.org/10.1175/MWR-D-10-05037.1.

Kusaka, H., Kimura, F., 2004. Coupling a single-layer urban canopy model with a simple atmospheric model: impact on urban heat island simulation for an idealized case. J. Meteorol. Soc. Jpn. 82, 67–80.

Kusaka, H., Kondo, H., Kikegawa, Y., 2001. A simple single-layer urban canopy model for atmospheric models: comparison with multi-layer and slab models. Bound.-Layer Meteorol. 101, 329–358. https://doi.org/10.1023/A:1019207923078.

Kusaka, H., Nawata, K., Suzuki-Parker, A., Takane, Y., Furuhashi, N., 2014. Mechanism of precipitation increase with urbanisation in Tokyo as revealed by ensemble climate simulations. J. Appl. Meteorol. Climatol. 53, 824–839. https://doi.org/10.1175/JAMC-D-13-065.1.

Kusaka, H., Nishi, A., Mizunari, M., Yokoyama, H., 2019. Urban impacts on spatiotemporal patterns of short-duration convective precipitation in a coastal city adjacent to a mountain. Q. J. R. Meteorol. Soc. 145, 2237–2254. https://doi.org/10.1002/qj.3555.

Landsberg, H.E., 1981. The Urban Climate. International Geophysics Series, Vol. 28. Academic Press, New York.

Lebakula, V., et al., 2025. LandScan global 30 arcsecond annual global gridded population datasets from 2000 to 2022. Sci. Data 12, 495. https://doi.org/10.1038/s41597-025-04817-z.

Li, J., Qian, Y., Leung, L.R., Feng, Z., Sarangi, C., Liu, Y., Yang, Z., 2022. Impacts of large-scale urbanization and irrigation on summer precipitation in the mid-Atlantic region of the United States. Geophys. Res. Lett. 49, e2022GL097845. https://doi.org/10.1029/2022GL097845.

Lin, C.-Y., Chen, W.-C., Liu, S.C., Liou, Y.A., Liu, G.R., Lin, T.H., 2008. Numerical study of the impact of urbanisation on the precipitation over Taiwan. Atmos. Environ. 42, 2934–2947. https://doi.org/10.1016/j.atmosenv.2007.12.054.

Lin, C.-Y., Chen, W.-C., Chang, S.C.P.-L., Sheng, Y.-F., 2011. Impact of the urban heat island effect on precipitation over a complex geographic environment in northern Taiwan. J. Appl. Meteorol. Climatol. 50, 339–353. https://doi.org/10.1175/2010JAMC2504.1.

Lin, C.-Y., Su, C.-J., Kusaka, H., Akimoto, Y., Sheng, Y.-F., Huang, J.-C., Hsu, H.-H., 2016. Impact of an improved WRF urban canopy model on diurnal air temperature simulation over northern Taiwan. Atmos. Chem. Phys. 16, 1809–1822. https://doi.org/10.5194/acp-16-1809-2016.

Miao, S., Chen, F., Li, Q., Fan, S., 2011. Impacts of urban processes and urbanisation on summer precipitation: a case study of heavy rainfall in Beijing on 1 August 2006. J. Appl. Meteorol. Climatol. 50, 806–825. https://doi.org/10.1175/2010JAMC2513.1.

Milbrandt, J.A., Yau, M.K., 2005a. A multimoment bulk microphysics parameterization. Part I: analysis of the role of the spectral shape parameter. J. Atmos. Sci. 62, 3051–3064. https://doi.org/10.1175/JAS3534.1.

Milbrandt, J.A., Yau, M.K., 2005b. A multimoment bulk microphysics parameterization. Part II: a proposed three-moment closure and scheme description. J. Atmos. Sci. 62, 3065–3081. https://doi.org/10.1175/JAS3535.1.

Mlawer, E.J., Taubman, S.J., Brown, P.D., Iacono, M.J., Clough, S.A., 1997. Radiative transfer for inhomogeneous atmospheres: RRTM, a validated correlated–k model for the longwave. J. Geophys. Res. Atmos. 102, 16663–16682. https://doi.org/10.1029/97JD00237.

Mohammad Hamray, N.S., Choi, M., 2022. Effects of heat waves on urban warming across different urban morphologies and climate zones. Build. Environ. 209, 108677. https://doi.org/10.1016/j.buildenv.2021.108677.

Moraglia, G., Crippa, P., 2026. Assessing the influence of aerosols on urban precipitation: a sensitivity study of Dallas–Fort Worth. Atmos. Res. 328, 108436. https://doi.org/10.1016/j.atmosres.2025.108436.

Moraglia, G., Pryor, S.C., Crippa, P., 2024. Quantifying the impacts of an urban area on clouds and precipitation patterns: a modeling perspective. J. Geophys. Res. Atmos. 129, e2024JD041402. https://doi.org/10.1029/2024JD041402.

Moriwaki, R., Watanabe, K., Morimoto, K., 2013. Urban dry island phenomenon and its impact on cloud base level. J. JSCE 1, 521–529. https://doi.org/10.2208/journalofjsce.1.1_521.

Morris, K.I., et al., 2016. Urbanisation and urban climate of a tropical conurbation, Klang Valley, Malaysia. Urban Clim. https://doi.org/10.1016/j.uclim.2016.12.002.

Morris, K.I., et al., 2017. Impact of urbanisation level on the interactions of urban area, the urban climate, and human thermal comfort. Appl. Geogr. 79, 50–72. https://doi.org/10.1016/j.apgeog.2016.12.007.

Morrison, H., Thompson, G., Tatarskii, V., 2009. Impact of cloud microphysics on the development of trailing Stratiform precipitation in a simulated squall line: comparison of one- and two-moment schemes. Mon. Weather Rev. 137, 991–1007. https://doi.org/10.1175/2008MWR2556.1.

Nakanishi, M., Niino, H., 2006. An improved Mellor-Yamada level 3 model: its numerical stability and application to a regional prediction of advection fog. Bound. Layer Meteorol. 119, 397–407. https://doi.org/10.1007/s10546-005-9030-8.

Nakanishi, M., Niino, H., 2009. Development of an improved turbulence closure model for the atmospheric boundary layer. J. Meteorol. Soc. Jpn. 87, 895–912. https://doi.org/10.2151/jmsj.87.895.

Niu .-Y., G., et al., 2011. The community Noah land surface model with multiparameterization options (Noah-MP): 1. Model description and evaluation with local-scale measurements. J. Geophys. Res. Atmos. 116 (D12). https://doi.org/10.1029/2010JD015139.

Niyogi, D., Lei, M., Kishtawal, C., Schmid, P., 2017. Urbanization impacts on the summer heavy rainfall climatology over the eastern United States. Earth Interact. 21, 1–17. https://doi.org/10.1175/EI-D-15-0045.1.

Oke, T.R., 1982. The energetic basis of the urban heat island. Q. J. R. Meteorol. Soc. 108, 1–24. https://doi.org/10.1002/qj.49710845502.

Ooi, M.C.G., Chan, A., Ashfold, M.J., Morris, K.I., Oozer, M.Y., Salleh, S.A., 2017. Numerical study on effect of urban heating on local climate during calm inter-monsoon period in Greater Kuala Lumpur, Malaysia. Urban Clim. 20, 228–250. https://doi.org/10.1016/j.uclim.2017.04.010.

Peixóto, J.P., Oort, A.H., 1992. Physics of Climate. American Institute of Physics, College Park, p. 520.

Pielke Sr., R.A., Pitman, A., Niyogi, D., Mahmood, R., McAlpine, C., Hossain, F., Goldewijk, K.K., Nair, U., Betts, R., Fall, S., Reichstein, M., Kabat, P., Noblet, N., 2011. Land use/land cover changes and climate: modelling analysis and observational evidence. WIREs Clim. Change 2, 783–934. https://doi.org/10.1002/wcc.144.

Pryor, S.C., Barthelmie, R.J., Zhou, X., Huffman, G.J., 2025. Re-examining urban rainfall enhancement over North America. Environ. Res. Lett. 20, 034035. https://doi.org/10.1088/1748-9326/adb507.

Public Sector Open Data, 2024. https://data.gov.my/data-catalogue (Accessed on 17 September 2024).

Quante, M., 2004. The role of clouds in the climate system. J. Phys. IV (Proc.) 121, 61–86. https://doi.org/10.1051/jp4:2004121003.

Ramakreshnan, L., Aghamohammadi, N., Fong, C.S., Ghaffarianhoseini, A., Wong, L.P., Sulaiman, N.M., 2019. Empirical study on temporal variations of canopy-level Urban Heat Island effect in the tropical city of Greater Kuala Lumpur. Sustain. Cities Soc. 44, 748–762. https://doi.org/10.1016/j.scs.2018.10.039.

Romanov, P., 1999. Urban influence on cloud cover estimated from satellite data. Atmos. Environ. 33, 4162–4172. https://doi.org/10.1016/S1352-2310(99)00159-4.

Rosenfeld, D., et al., 2014. Global observations of aerosol-cloud-precipitation-climate interactions. Rev. Geophys. 52, 750–808. https://doi.org/10.1002/2013RG000441.

Scian, B., Labraga, J.C., Reimers, W., Frumento, O., 2006. Characteristics of large-scale atmospheric circulation related to extreme monthly rainfall anomalies in the Pampa region, Argentina, under non-ENSO conditions. Theor. Appl. Climatol. 85, 89–106. https://doi.org/10.1007/s00704-005-0182-8.

Shariff, A.R.M., et al., 2015. A preliminary study of cold surges and precipitation during the northeast monsoon season over Malaysia. Adv. Sci. Lett. 21, 185–188. https://doi.org/10.1166/asl.2015.5851.

Shepherd, J.M., 2005. A review of current investigations of urban-induced rainfall and recommendations for the future. Earth Interact. 9, 1–27. https://doi.org/10.1175/EI156.1.

Shepherd, J.M., Stallins, J.A., Jin, M.L., Mote, T.L., 2010. Urbanisation: impacts on clouds, precipitation, and lightning. Urban Ecosyst. Ecol. 55, 1. https://doi.org/10.2134/agronmonogr55.c1.

Skamarock, W.C., et al., 2019. A description of the Advanced Research WRF Version 4. In: NCAR Technical Notes NCAR/TN-556+STR, p. 145. https://doi.org/10.5065/1dfh-6p97.

Stephens, G.L., 2005. Cloud feedbacks in the climate system: a critical review. J. Clim. 18, 237–273. https://doi.org/10.1175/JCLI-3243.1.

Sui, X., Yang, Z.-L., Shepherd, M., Niyogi, D., 2024. Global scale assessment of urban precipitation anomalies. Proc. Natl. Acad. Sci. 121, 1091–6490. https://doi.org/10.1073/pnas.2311496121.

Syed Mahbar, S.F., Kusaka, H., 2024a. Urbanisation increases cloudiness over Greater Kuala Lumpur during southwest and northeast monsoons. Weather 80, 144–151. https://doi.org/10.1002/wea.7644.

Syed Mahbar, S.F., Kusaka, H., 2024b. Synergistic interactions between urban heat islands and heat waves in the Greater Kuala Lumpur and surrounding areas. Int. J. Climatol. 44, 4886–4906. https://doi.org/10.1002/joc.8614.

Tangang, F., et al., 2017. Characteristics of precipitation extremes in Malaysia associated with El Niño and La Niña events. Int. J. Climatol. 37, 696–716. https://doi.org/10.1002/joc.5032.

Tangang, F., et al., 2020. Projected future changes in rainfall in Southeast Asia based on CORDEX–SEA multi-model simulations. Clim. Dyn. 55, 1247–1267. https://doi.org/10.1007/s00382-020-05322-2.

Theeuwes, N.E., Barlow, J.F., Teuling, A.J., Grimmond, C.S.B., Kotthaus, S., 2019. Persistent cloud cover over mega-cities linked to surface heat release. Npj Clim. Atmos. Sci. https://doi.org/10.1038/s41612-019-0072-x.

Theeuwes, N.E., Boutle, I.A., Clark, P.A., Grimmoind, S., 2022. Understanding London's summertime cloud cover. Q. J. R. Meteorol. Soc. 148, 454–465. https://doi.org/10.1002/qj.4214.

Thompson, G., Field, P.R., Rasmussen, R.M., Hall, W.D., 2008. Explicit forecasts of winter precipitation using an improved bulk microphysics scheme. Part II: implementation of a new snow parameterization. Mon. Weather Rev. 136, 5095–5115. https://doi.org/10.1175/2008MWR2387.1.

Varquez, A.C.G., Kiyomoyo, S., Khanh, D.N., Kanda, M., 2021. Global 1-km present and future hourly anthropogenic heat flux. Sci. Data 8, 64. https://doi.org/10.1038/s41597-021-00850-w.

Vo, T.T., Hu, L., Xue, L., Li, Q., Chen, S., 2023. Urban effects on cloud patterns. Proc. Natl. Acad. Sci. 120, e2216765120. https://doi.org/10.1073/pnas.2216765120.

Xu, K.-M., Randall, D.A., 1996. A semiempirical cloudiness parameterization for use in climate models. J. Atmos. Sci. 53, 3084–3102. https://doi.org/10.1175/1520-0469(1996)053%3C3084:ASCPFU%3E2.0.CO;2.

Yang, Z.-L., et al., 2011. The community Noah land surface model with multiparameterization options (Noah-MP): 2. Evaluation over global river basins. J. Geophys. Res. Atmos. 116, D12. https://doi.org/10.1029/2010JD015140.

Yasin, M.Y., Mohd Zain, M.A., Hassan, M.H., 2022. Urbanisation and growth of Greater Kuala Lumpur: issues and recommendations for urban growth management. Southeast Asia 22, 4–19. https://doi.org/10.1108/SEAMJ-02-2022-B1002.

Yusof, M.S.M., 2022. Peningkatan Model Ramalan Cuaca Numerikal dari 3-Hari Kehadapan dengan Resolusi 4km kepada 4-Hari Kehadapan dengan Resolusi 3km bagi Seluruh Malaysia. Malaysian Meteorological Department. ISBN/ISSN:ISBN :978-967-2327-08-0.

Zhang, C., Wang, Y., 2017. Projected future changes of tropical cyclone activity over the Western North and South Pacific in a 20-km-mesh regional climate model. J. Clim. 30, 5923–5941. https://doi.org/10.1175/JCLI-D-16-0597.1.

Zhang, W., Yang, J., Yang, L., Niyogi, D., 2022. Impacts of City shape on rainfall in inland and coastal environments. Earth's Future 10, e2022EF002654. https://doi.org/10.1029/2022EF002654.

Zhou, X., Letson, F., Crippa, P., Pryor, S.C., 2024. Urban effect on precipitation and deep convective systems over Dallas-Fort Worth. J. Geophys. Res. Atmos. 129, e2023JD039972. https://doi.org/10.1029/2023JD039972.